

Recent Progress on Transition Metal Oxides as Bifunctional Catalysts for Lithium-Air and Zinc-Air Batteries

Jing Pan,^[a, b] Xin Long Tian,^[a] Shahid Zaman,^[a] Zehua Dong,^[a] Hongfang Liu,^[a] Ho Seok Park,^{*[b]} and Bao Yu Xia^{*[a]}

In recent years, rechargeable Li-air and Zn-air batteries have attracted wide attention due to their high theoretical specific energy densities. However, the high cost and poor stability of noble metal catalysts for the oxygen redox reactions limit their practical large-scale application. On contrast, low-cost transition metal oxide (TMO)-based composite materials exhibit considerable bifunctional activity for oxygen reduction and oxygen evolution, and excellent stability, which holds great potential over the precious metal-based catalysts. This work briefly introduces the recent advances in TMO-based composites as

bifunctional oxygen electrocatalysts for Li-air and Zn-air batteries. After a brief introduction into the research field of air batteries, metal oxides (including Co- and Mn-based oxides) and polymetallic oxides (mainly spinel and perovskite types) are reviewed. In consideration of the poor electronic conductivity of metal oxide catalysts, composites including additional conductive materials are also introduced. Finally, challenges and perspectives of bifunctional TMOs are emphasized to stimulate innovations for the future development of practical Li-air and Zn-air batteries.

1. Introduction

The ever-increasing energy consumption and related environmental problems generate an increasing demand for renewable and environmental-friendly energy source as a substitute for traditional fossil fuels.^[1,2] Due to their super-high energy densities and the ability to be recharged, secondary metal-air batteries are promising candidates as next generation energy storage and conversion devices.^[3] Based on the metal anode used, the devices are classified as lithium-air (Li-air), sodium-air (Na-air), potassium-air (K-air), zinc-air (Zn-air), iron-air (Fe-air), magnesium-air (Mg-air), and aluminum-air (Al-air) batteries.^[4] Among these, Li-air and Zn-air batteries show the most promising potential for applications in future portable electronics and vehicles due to their large theoretical specific energy density.^[5–8]

The underlying working mechanism of Li-air and Zn-air batteries is similar. Both are based on metal centered redox reactions at the metal electrode and oxygen redox reactions at

the air electrode.^[9] At the air electrode, the oxygen reduction reaction (ORR) takes place during discharge, oxidizing the metal at the counter electrode. During the charging process, the oxygen evolution reaction (OER) takes place at the cathode and metal ions are reduced at the metal electrode. Efficient catalysis of ORR and OER is critical for the efficiency of the whole cell.^[10,11] Until now, composites based on precious metals are the most commonly used electrocatalysts for ORR and OER in such devices.^[12,13] Despite their excellent catalytic activity, the large scale application of such composites is restricted by their high cost and lower stability.^[14,15] Consequently, it is of great significance to investigate alternative catalysts based on non-noble metals with a comparable catalytic performance but a more economical price.^[16] Carbon-based materials,^[17] transition metal oxides (TMOs),^[18] phosphides,^[19] and nitrides^[20] are the most extensively investigated non-noble metal oxygen electrocatalysts for metal-air batteries.^[21] However, under the high potential required for the electric auxiliary OER process these materials, except of the transition metal oxides, are easily oxidized or hydroxylized, which inevitably results in the decline of battery performance.^[22] In addition, acceptable price, abundant reserves, and reasonable catalytic activity of TMOs further promote their development.^[23]

The activity of the catalysts is usually tested utilizing rotating disk electrodes. However, for the practical development of TMOs as efficient bifunctional oxygen catalysts in metal-air batteries, the real performance of batteries under practical environmental condition also has to be evaluated.^[24–26] Typical cathode reactions for Li-air batteries involve the formation of various lithium oxides.^[27] For the fabrication of air electrodes, poly(vinylidene fluoride) (PVDF) as a binder and carbon based materials are commonly used. The intermediate product of LiO_2 and Li_2O_2 can react with PVDF and the carbon based materials, leading to a severe stability decay of the

[a] Dr. J. Pan, Dr. X. L. Tian, S. Zaman, Prof. Z. Dong, Prof. H. Liu, Prof. B. Y. Xia
Key Laboratory of Material Chemistry for Energy Conversion and Storage
(Ministry of Education)

Hubei Key Laboratory of Material Chemistry and Service Failure
School of Chemistry and Chemical Engineering
Wuhan National Laboratory for Optoelectronics
Huazhong University of Science and Technology (HUST)
1037 Luoyu Road, Wuhan 430074, P. R. China
E-mail: byxia@hust.edu.cn

[b] Dr. J. Pan, Prof. H. S. Park
School of Chemical Engineering
Sungkyunkwan University
2066 Seobu-ro, Jangan-gu, Suwon-si, Gyeonggi-do, 440-746, Republic of Korea
E-mail: phs0727@skku.edu
An invited contribution to a Special Issue on Bifunctional Catalysts for Metal-Air Batteries

battery.^[28,29] Additionally, the high potential gap in Li-air batteries (> 1 V) could cause serious carbon corrosion during the charging/discharging process.^[30] Therefore, TMO electrocatalysts in Li-air batteries should be directly grown on the surface of a current collector and binder-free electrodes without corrosive carbon materials are required. For Zn-air batteries, the performance of TMO electrocatalysts is affected by the alkaline electrolyte. It is worth mentioning that carbonate precipitation can also easily take place in alkaline media ($\text{CO}_2 + 2\text{OH}^- \rightarrow \text{CO}_3^{2-} + \text{H}_2\text{O}$), blocking the pores and channels of the electrode, decreasing the accessibility of the active catalyst surface, reducing the electrical conductivity of the electrode,^[31] and thus, drastically lowering the battery performance.^[32] In consequence, the formation and adsorption of carbonate precipitates at the electrocatalysts should be minimized.

Also the device configuration of metal-air batteries can affect the electrochemical performance of the oxygen electrocatalysts. In contrast to traditional metal-air batteries, a good mechanical deformability is required for air electrodes in flexible metal-air batteries.^[33] Conventional rigid substrates, such as carbon papers, are thus not suitable as a supporting material for loading the TMO electrocatalysts in flexible batteries.

In order to address the described challenges, TMOs and their composites have been extensively investigated to develop competitive ORR and OER electrocatalysts for high-performance metal-air batteries beyond precious metals.^[34] Since the rapid development in this field, the review of TMOs is timely urgent and imperative for the design of future bifunctional catalysts in metal-air batteries. Even though bifunctional oxygen catalysts in Zn-air batteries have been reviewed in several prominent articles,^[35,36] the introduction of TMOs specifically as bifunctional oxygen catalysts in Li-air and Zn-air batteries is yet to be spotlighted. Therefore, this review focuses solely on bifunctional TMOs for application in Li-air and Zn-air batteries. First of all, TMO nanomaterials will be profiled, focusing on Co and Mn-based oxides as bifunctional catalysts. Furthermore, this work will briefly study the multicomponent TMOs (spinel and perovskite types) and hybrid composites with carbon materials. Finally, the perspectives and insights will be concluded. It is anticipated that this brief review will offer valuable perceptions for future research and help to direct the advanced bifunctional TMOs for practical metal-air batteries.

2. Single Metal Oxides

The abundant nature of transition metals and their oxides has great potential for optimizing the electrochemical performance.^[37] To identify suitable candidates as efficient electrocatalysts out of this class of materials, the detailed reaction mechanism has been investigated. For the ORR process, metal-air batteries display two types of reactions, proceeding via a dissociative or associative pathway.^[38] The OER process can be regarded as the backreaction of ORR, following the reverse direction. ORR and OER are commonly limited by proton coupled electron transfer steps to O^* or OH^* species (* is labelling surface sites at the electrode).^[39]

As a result of these studies, Co_3O_4 , NiO , and MnO_2 , except of precious metal oxides, have been identified as the most promising candidates as OER electrocatalysts (Figure 1). How-

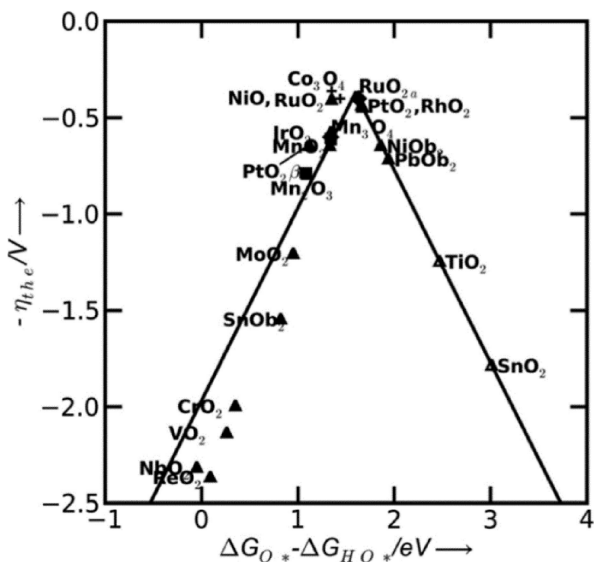


Figure 1. Theoretical overpotentials for OER compared to difference between the standard free energy of O^* and HO for single transition metal oxides. Reproduced with permission.^[39] Copyright 2011, Wiley.

ever, despite its excellent OER performance, NiO has a poor ORR activity and stability in the electrochemical experiments and in air battery tests.^[40–42] Hence, Co and Mn-based single metal oxides are the core topics of this section.

2.1. Cobalt Oxides

Cobalt oxides (CoO_x) are promising candidates for metal-air batteries in view of their outstanding bifunctional catalytic activity, especially the spinel type oxide Co_3O_4 .^[43] For a typical spinel type structure of Co_3O_4 , Co^{2+} and Co^{3+} ions occupy tetrahedral and octahedral sites, respectively.^[44] It has been reported that catalysts with Co^{2+} enriched surface exhibit better ORR performance, while the OER activity benefits from a higher number of Co^{3+} sites at the surface.^[45] The enhanced activity might be explained by the improved adsorption of O_2 and OH^- at Co^{2+} and Co^{3+} sites, respectively.^[46] Consequently, the surface arrangement of Co^{2+} and Co^{3+} ions of Co_3O_4 electrocatalysts should be carefully designed and investigated to optimize bifunctional catalytic activity. As pointed out by some researchers, Co_3O_4 polyhedrons enclosed by {112} facets exhibit higher bifunctional activities for ORR and OER compared to octahedrons enclosed predominantly by {001} and {001} + {111} facets, respectively. The result is proposed to the optimized ratio of $\text{Co}^{2+}/\text{Co}^{3+}$ active sites and presence of the octahedral coordinated Co^{3+} ions.^[47]

Doping is a similarly effective strategy to further enhance the activity of Co_3O_4 . It has been revealed experimentally and by density functional theory (DFT) calculations that nitrogen (N)

doping into the skeleton of Co_3O_4 can improve the electron conductivity, O_2 adsorption ability, and ORR kinetics.^[48] Doping accomplished by thermal treatment of Co_3O_4 nanostructures under ammonia gas proposed the presence of stacking faults (Figure 2a), which could be additional catalytic sites for the electrocatalysis in N-doped Co_3O_4 nanowires. Apart from that, the annealing temperature has a significant impact on the ORR performance of N-doped Co_3O_4 nanowires. A Sample treated at 200 °C (N2-Co₃O₄) exhibited the most positive onset potential of 0.94 V (vs. RHE) among samples systematically treated at 100~400 °C (Figure 2b). When assembled into Zn-air batteries, the N-doped samples also revealed a higher peak power density (32.0 mW cm⁻³ at 90 mA cm⁻³) than undoped samples (14.7 mW cm⁻³ at 35.6 mA cm⁻³) (Figure 2c). It has also been shown that magnesium (Mg) doping into Co_3O_4 can improve the bifunctional activity, resulting from higher electrical con-

ductivity and the existence of lattice buffer zones with enhanced hydroxyl detachment.^[49]

Creating oxygen vacancies on the specific surface of Co oxides has also been demonstrated to have a similarly positive effect. Qiao et al. reported improved bifunctional activity of CoO nanorods by creating oxygen vacancies on the oxygen-terminated {111} face of CoO nanorods.^[50] The comparison of ORR and OER performance of the surface engineered CoO nanorods and pristine ones directly shows the effectiveness of introducing oxygen vacancies (Figure 2d-f). As indicated by DFT calculations, the introduction of oxygen vacancies on the surface of Co_3O_4 could lead to new gap states and the electrons previously localized in Co–O bonds turn to be more delocalized. These changes eventually lead to an improved electrical conductivity and electrocatalytic performance.^[51]

Compared to the controlled conditions of the electrochemical measurements of the ORR and OER activity in model

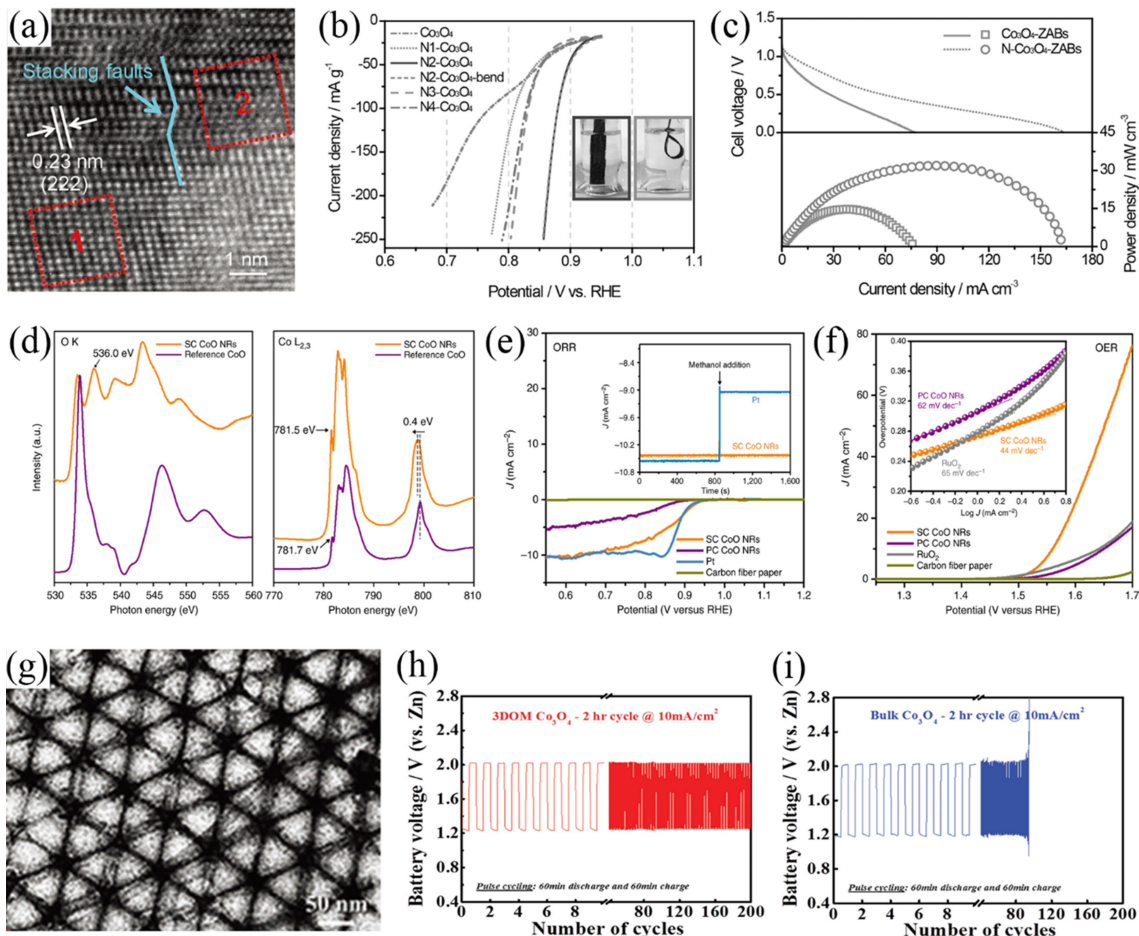


Figure 2. a) HRTEM image of N₂-Co₃O₄ nanowires. b) IR-corrected LSV curves of N-doped Co₃O₄ nanowires treated at different temperatures. The tests were held in O₂-saturated 1 M KOH electrolyte. N1~N4-Co₃O₄ represent N-doped Co₃O₄ nanowires treated at 100~400 °C, respectively. c) Polarization curves and corresponding power density plots of Co₃O₄ and N₂-Co₃O₄ based Zn-air batteries. The electrolyte used in the Zn-air batteries was alkaline gel electrolyte employing polyvinyl alcohol (PVA). Reproduced with permission.^[48] Copyright 2017, Wiley. d) O–K edge and Co-L_{2,3} edge XANES spectra of SC and reference CoO, respectively. The peak at about 536 eV for SC CoO in the O–K edge is attribute to O deficiency. In the Co-L_{2,3} edge part, the peaks at ~781.5 and 800 eV of SC CoO moved towards low photon energy direction compared to the CoO, suggesting the electron transformation from O-vacancies to Co d band. The ORR (e) and OER (f) performances of the SC and PC CO nanorods in O₂-saturated 1 M KOH solution. Reproduced with permission.^[50] Copyright 2016, Nature. g) TEM image of the 3DOM Co₃O₄. The galvanostatic charge and discharge properties for the Zn-air batteries fabricated by 3DOM (h) and bulk Co₃O₄ (i), respectively. As electrolyte for the Zn-air batteries, 6.0 M KOH solution with 0.2 M zinc acetate was used. Reproduced with permission.^[53] Copyright 2016, Wiley.

experiments, metal-air batteries are open systems with advanced requirements for efficient oxygen catalysts, including large porosity and high active surface area.^[52] The reasons are as follows: (1) the reduction products formed at the metal electrode during the discharging process need significant space for their deposition, particularly in case of Li-air batteries; (2) the oxygen redox reactions take place at a three-phase interface between gas, liquid, and solid. A sufficient three-phase interface can be facilitated by ensuring effective contact of air and electrolyte with the electrocatalysts; (3) porosity of the catalysts is also beneficial to the continuous supply of air and for mass transport of electrolyte during the reaction. For instance, Chen et al. employed polystyrene (PS) as a template to obtain three-dimensional ordered porous Co_3O_4 (Figure 2g).^[53] The catalyst exhibited large porosity with regular pores of ~ 150 nm, a large specific surface area of $44.7 \text{ m}^2 \text{ g}^{-1}$ (contrast to $8.52 \text{ m}^2 \text{ g}^{-1}$ of bulk Co_3O_4) and robust structure. The Zn-air battery based on this electrocatalyst revealed a much

higher stability of 200 cycles and 400 h compared with the bulk Co_3O_4 (Figure 2h–i).

2.2. Manganese Oxides

Manganese oxides (MnO_x) also show robust catalytic activity for both ORR and OER.^[54] The larger reserves of manganese compared to cobalt further increases the potential for practical application of MnO_x based materials.^[55] The most frequently investigated class of manganese oxides is manganese dioxide (MnO_2), for which the bifunctional activity strongly depends on the crystal phase of the distinct oxide.^[56] The ORR and OER performance show similar trends and the activity follows the order of $\alpha\text{-MnO}_2 >$ amorphous $\text{MnO}_2 > \beta\text{-MnO}_2 > \delta\text{-MnO}_2$ (Figure 3a). However, this order is not absolute as the activity of MnO_x based electrocatalysts can be affected by various factors including morphology, structure, nature of electrolyte and so on. For instance, a Li-air battery fabricated using $\beta\text{-MnO}_2$

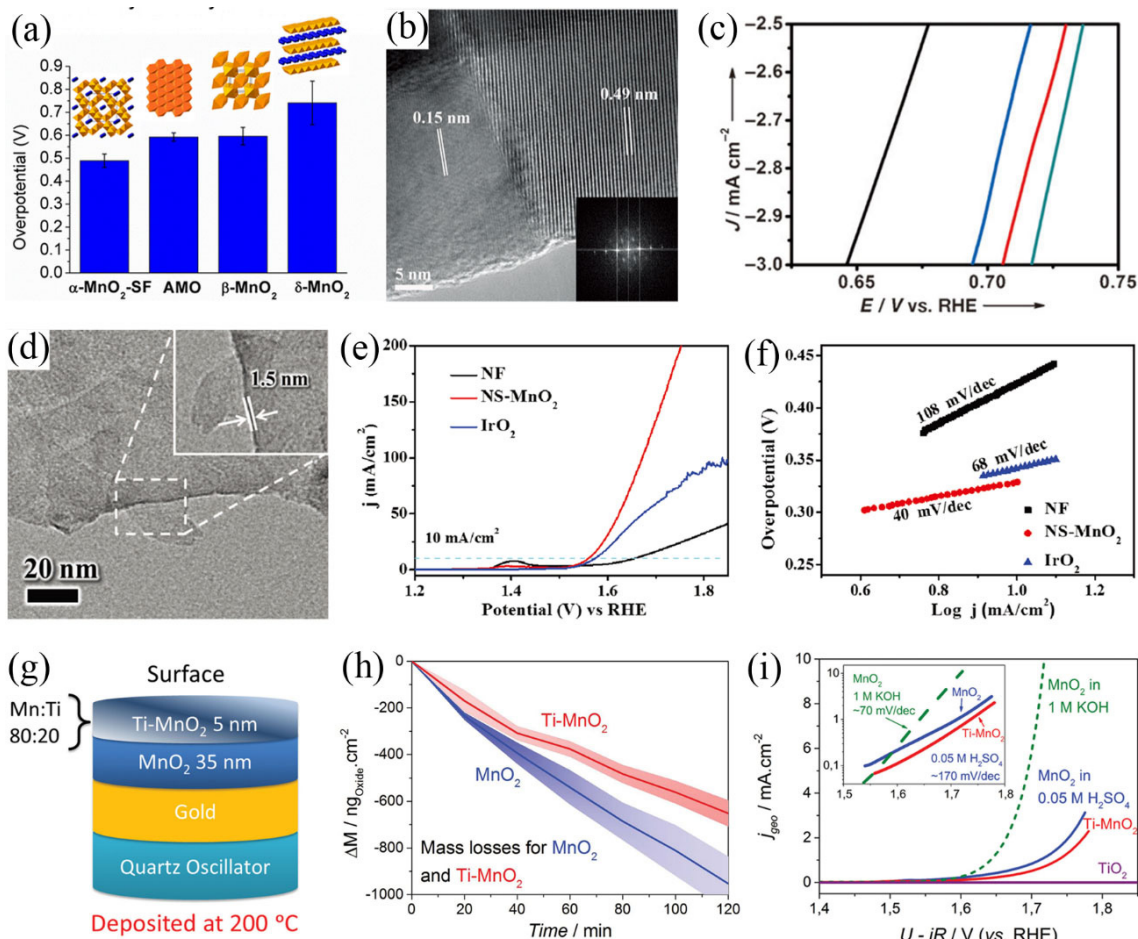


Figure 3. a) Overpotentials at 10 mA cm^{-2} for MnO_2 with different crystal structures. Reproduced with permission.^[56] Copyright 2014, ACS. b) HRTEM images of $\beta\text{-MnO}_2$ heated in Ar. c) Specific activities around the half-wave potential area in 0.1 M KOH saturated with O_2 . The black, red, blue, and green lines represent the pristine, Ar treated at 350°C for 2 h, Ar treated at 350°C for 4 h, and Air treated at 400°C for 2 h $\beta\text{-MnO}_2$. Reproduced with permission.^[58] Copyright 2013, Wiley. d) TEM image of the $\delta\text{-MnO}_2$ nanosheets. LSV curves (e) and Tafel plots (f) for OER of bare nickel foam (NF), nickel foam loaded with $\delta\text{-MnO}_2$ nanosheets (NS-MnO₂) and commercial IrO₂ in 1 M KOH . Reproduced with permission.^[61] Copyright 2017, Wiley. g) Schematic graph for the Ti ion-doped MnO₂ (Ti-MnO₂) electrode. Mass change during the electrochemical tests (h) and OER performance (i) of the Ti ion-doped and primary MnO₂ electrodes. The LSV curves measured in 1 M KOH solution and in $0.05 \text{ M H}_2\text{SO}_4$ were shown in green and blue, respectively. Reproduced with permission.^[63] Copyright 2017, Wiley.

nanowires in aprotic electrolyte presented a larger discharge capacity ($\sim 2500 \text{ mAh g}^{-1}$) than a cell using $\alpha\text{-MnO}_2$ nanowires.^[57]

Similar to cobalt oxides, generating vacancies at the MnO_2 surface is an effective strategy to modify interactions with oxygen-based species during the redox reactions for enhancing the ORR activity.^[58] Native oxygen defects on the surface of $\beta\text{-MnO}_2$ can be introduced by heat treatment in Ar atmosphere (Figure 3b). Compared to heat treatment in air, the $\beta\text{-MnO}_2$ crystal with oxygen vacancies exhibited an enhanced ORR activity (Figure 3c). Cationic doping has also been proposed to be beneficial for the ORR performance of MnO_2 .^[59] The electron transfer value (n) during the ORR has been improved for nickel ($n=3.6$) and copper ($n=3.5$) doped MnO_2 , while the pristine MnO_2 nanowires showed a lower value ($n=3.0$).

In general, the ORR performance of MnO_2 is usually higher than its OER performance.^[60] Thus, improving the OER activity is of the utmost importance in order to improve the overall performance. It has been demonstrated recently, that the vacancy defect engineering method has a positive influence on the OER activity of $\delta\text{-MnO}_2$. $\delta\text{-MnO}_2$ ultrathin nanosheets (NS-MnO_2) grown on the surface of nickel foam (Figure 3d) were prepared, containing a high number of oxygen vacancies, resulting in the presence of a high number of Mn^{3+} active sites showing strong H_2O adsorption.^[61] The catalyst material exhibits a low overpotential and a smaller Tafel slope, even lower than observed for commercial IrO_2 (Figure 3e and f).

The activity of MnO_2 based catalysts is pH-dependent, as surface active Mn^{3+} ions transform into Mn^{2+} and Mn^{4+} in electrolytes with a pH < 9.^[62] Acid leaching from uncoordinated sites has thus to be hindered to improve the durability of MnO_2 in acidic media. Ifan E. L. Stephens decorated undercoordinated surface sites with stable Ti ions on the MnO_2 surface by sputter-deposition (Figure 3g).^[63] This addition lead to improved stability of MnO_2 (Figure 3h), along with better OER activity in acidic electrolytes (Figure 3i).

Other Mn oxides also showed excellent catalytic activity. For instance, Mn_2O_3 expresses a bifunctional activity even better than that observed for MnO_2 and Mn_3O_4 .^[64,65] However, this catalyst exhibits very low stability because it can be easily oxidized.^[66] That necessitates the synchronization of catalytic activity and stability for this kind of electrocatalyst.

In practice, supporting materials are often employed to further improve the catalytic performance. For instance, Co and Mn oxide nanoparticles grown on the surface of porous silica scaffolds can achieve a higher amount of surface metal sites vs area resulting enhanced battery stability.^[67] Introducing different kinds of atoms into the MnO_x electrocatalysts is also frequently employed to improve the metal-air battery performance. For example, a Li_2MnO_3 composite was synthesized by inserting Li^+ into R-MnO_2 (Ramsdellite). By theoretical calculation, this insertion was shown to optimize the O_2 redox reaction kinetics as well as the decomposition of produced Li_2O_2 . The fabricated Li-O_2 battery can reveal a large capacity of 5000 mAh g^{-1} .^[68]

3. Polymetallic Oxides

Given that more active sites can be introduced by additional metal ions, polymetallic oxides are expected to show higher intrinsic activity than single metal oxides for oxygen electrochemistry.^[69] Furthermore, the activity of single metal oxides can be easily optimized via the modulation of crystalline structure, valence and electronic states of either metal element.^[70] This section will highlight bifunctional catalysts of polymetallic spinel and perovskite oxides addressing their excellent performance and prevalent use in electrocatalysis and metal-air batteries.

3.1. Spinel Oxides

Typical spinel polymetallic oxides show a composition of the formula $\text{A}_x\text{B}_{3-x}\text{O}_4$. The structure is created by a cubic unit cell containing 8 tetragonal subunits.^[37] Abundant disordered sites are present caused by the cation arrangement.^[44] The tiny structural changes directly respond to the electronic structure and the adsorption ability of oxygen related groups,^[58] also influencing the ORR and OER properties. For example, the structure of spinel cobalt manganese oxides ($\text{Co}_{3-x}\text{Mn}_x\text{O}_4$) can be adjusted by the Mn content. At large Mn percentages ($1.9 \leq x \leq 3$), the crystallographic structure shows the tetragonal phase, while for small Mn percentages ($0 \leq x \leq 1.3$), the cubic spinel crystallographic structure is present (Figure 4a). Based on the same mechanism, CoMnO-P (mainly in cubic phase), CoMnO-B (tetragonal phase), HT-T-spinel (tetragonal CoMn_2O_4), and HT-C-spinel (cubic Co_2MnO_4) are prepared.^[71] The ORR catalytic activity order is shown as, $\text{CoMnO-P} > \text{CoMnO-B} > \text{HT-C-spinel} > \text{HT-T-spinel}$ (Figure 4b). In general, spinel oxides showing a cubic structure performed better in terms of catalytic activity than spinels of the tetragonal structure. The OER performance follows a different trend of $\text{CoMnO-B} > \text{CoMnO-P} > \text{HT-T-spinel} > \text{HT-C-spinel}$ (Figure 4c), suggesting that the tetragonal structures exhibit properties leading to a higher catalytic activity than observed for the cubic structures. This phase and composition co-dependent activity is verified for Co-Mn and Co-Fe spinel nanoparticles by reversing their structure based on various Co/Fe content.^[72-74]

Considering the outstanding catalytic activity and corrosion stability of Co-based spinel oxides in basic electrolyte, these are the most attractive spinel type bifunctional oxygen catalysts.^[4] Besides $\text{Co}_{3-x}\text{Mn}_x\text{O}$ mentioned above, NiCo_2O_4 is also extensively studied. Chen and co-workers synthesized porous NiCo_2O_4 microspheres constructed of porous nanosheets. When assembled into Li-O_2 batteries, the battery displayed a discharging/charging voltage gap of 1.23 V and a capacity of 6822 mAh g^{-1} _{carbon} at 200 mA g^{-1} _{carbon}.^[75] Similarly, a hierarchical nanostructured NiCo_2O_4 shows a decent performance for Zn-air batteries with a discharge capacity of $\sim 580 \text{ mA h g}^{-1}$.^[76] It has been mentioned earlier that the corrosion under the high potential of OER process is a major challenge for ORR catalysts. This problem can be avoided by employing a decoupled electrode configuration in the fabrication of Li-air batteries. For

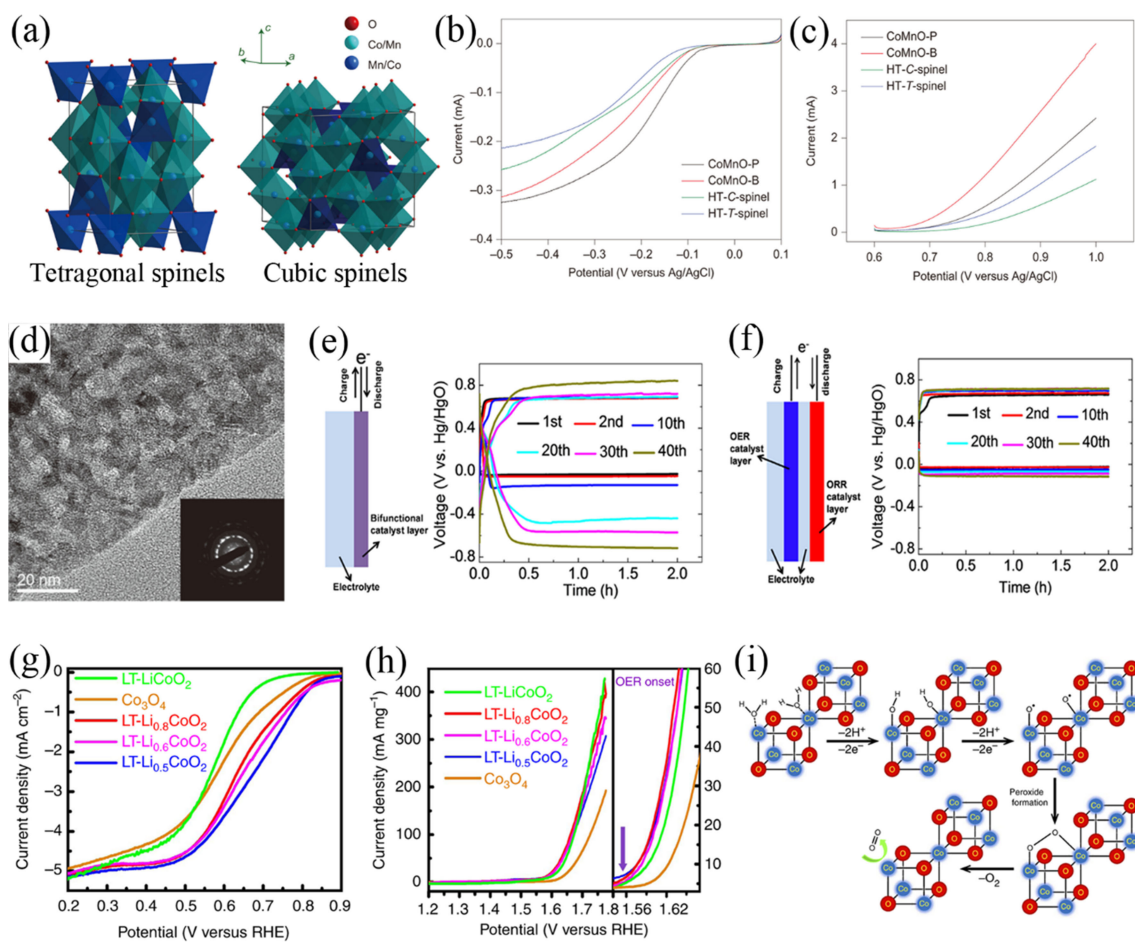


Figure 4. a) Schematic representation of tetragonal and cubic spinels. LSV curves of the ORR (b) and OER (c) tests of nanocrystalline CoMnO–B, CoMnO–P, HT–C–spinel and HT–T–spinel in 0.1 M KOH. Reproduced with permission.^[71] Copyright 2011, Nature. d) TEM image of NiCo₂O₄ nanoflakes. Cycling performances of the various configurations for Li–air batteries at 2.0 mA cm^{−2}; e) single, and f) decoupled air electrodes. The electrolyte employed was a mixture aqueous solution of 0.5 M LiOH and 1 M LiNO₃. Reproduced with permission.^[77] Copyright 2014, Elsevier. ORR (g) and OER (h) activities of LT-Li_{1-x}CoO₂ for 0 ≤ x ≤ 0.5 in comparison with Co₃O₄ in 0.1 M KOH. i) Mechanism of OER on Co₄O₄ cubane units in LT-LiCoO₂. Reproduced with permission.^[78] Copyright 2014, Nature.

instance, adopting nickel foam with NiCo₂O₄ nanosheets (Figure 4d) grown on the surface as OER electrode and a carbon paper loaded with Pt/C as ORR electrode. Compared with the traditional electrode configuration, this configuration achieved a much higher stability (Figure 4e and f).^[77]

LiCoO₂, an intensively investigated active material for Li-ion batteries, has also been studied as electrocatalyst for Li–air batteries. Although the observed ORR activity was not very promising, the partly delithiated product of LiCoO₂, Li_{0.5}CoO₂, exhibited a surprisingly good activity for both ORR and OER (Figure 4g and h). The results were explained by the presence of Co₄O₄ cubane subunits in Li_{0.5}CoO₂ and a pinning of the Co³⁺/⁴⁺: 3d energy with the top of the O²⁻: 2p band (Figure 4i).^[78] In addition, other Co-based oxide structures such as FeCo₂O₄ porous nanorods and CuCo₂O₄ nanoparticles were also reported as efficient bifunctional electrocatalysts for Li–O₂ and Li–air batteries.^[79,80]

The preparation process of an electrocatalyst strongly influences its morphology and, consequently, its catalytic activity. For example, NiMn₂O₄ made via ball-milling exhibited a

larger specific surface area and thus, a higher number of accessible active sites, and as a result, it displayed a better Li–air battery performance compared to the corresponding product prepared by precipitation.^[81] Tubular CoMn₂O₄ nanostructures prepared by electrospinning exhibited a much larger specific surface area as well as a smaller and more uniform crystallite size (10 nm) compared to CoMn₂O₄ nanostructures prepared via traditional annealing process at high temperature.^[82,83] The specific capacity of Li–O₂ battery assembled with CoMn₂O₄ tube nanostructures was 5355 mAh g⁻¹ carbon at 100 mA g⁻¹ carbon. More importantly, the tube structures of CoMn₂O₄ not only facilitated accommodation of the generated Li₂O₂ product but could also be recovered after the charging process. Thus, addition of CoMn₂O₄ nanostructures lead to an increased recyclability of the battery to more than 100 cycles from the initial 20 cycles.

3.2. Perovskite Oxides

Perovskite oxides have been recognized as significant OER catalysts. Although the ORR activity of these materials is very low compared to their OER activity, it has been greatly improved in recent years. In general, perovskite oxide composites show a ABO_3 structure, where A is a rare earth or alkali element, and B represents the transition metal.^[84] Compared with A sites, the metal ions at the B sites have a higher impact on the band gap of perovskite materials.^[85] For the application in electrocatalysis, the B site is also recognized as catalytically active center.^[86] Yang et al. demonstrated that both ORR and OER properties of perovskite oxides are dependent on the σ -orbital (e_g) occupation and B site metal-oxygen covalence (Figure 5a).^[87,88] When improving the filling of e_g -orbital antibonding states for the B site metal to near 1, the covalence of the B–O bond can be simultaneously enhanced, leading to a better ORR and OER activity. The ORR and OER performance for

a series of perovskite oxides are listed to illustrate this relationship (Figure 5b and c). Based on these principles, a series of double perovskite oxide $\text{PrBa}_{0.5}\text{Sr}_{0.5}\text{Co}_{1.5}\text{Fe}_{0.5}\text{O}_{5+\delta}$ (PBSCF) nanofibers were prepared, which showed robust OER activity (Figure 5d–f).^[89,90] By co-doping of strontium (Sr) and iron (Fe) into $\text{PrBaCo}_{2+\delta}$ (PBC-0) a larger specific surface area as well as a favorable e_g electron filling was achieved. A similar work on mesoporous $\text{PrBa}_{0.5}\text{Sr}_{0.5}\text{Co}_{2-x}\text{Fe}_x\text{O}_{5+\delta}$ nanofibers has been published recently.^[90]

Decreasing binding of oxygenated species on the surface of the B site has been shown to enhance the catalytic activity of perovskite oxides.^[91] For example, by increasing the amount of the surface Mn^{4+} proportion in mesoporous $\text{LaMnO}_{3+\delta}$ perovskite spheres (Figure 5g–j), the ORR activity was greatly improved and even comparable to a commercial Pt/C catalyst (Figure 5k).^[92] When used to assemble Zn-air batteries, an open-circuit voltage of 1.43 V and a power density of 198.6 mW cm^{-2}

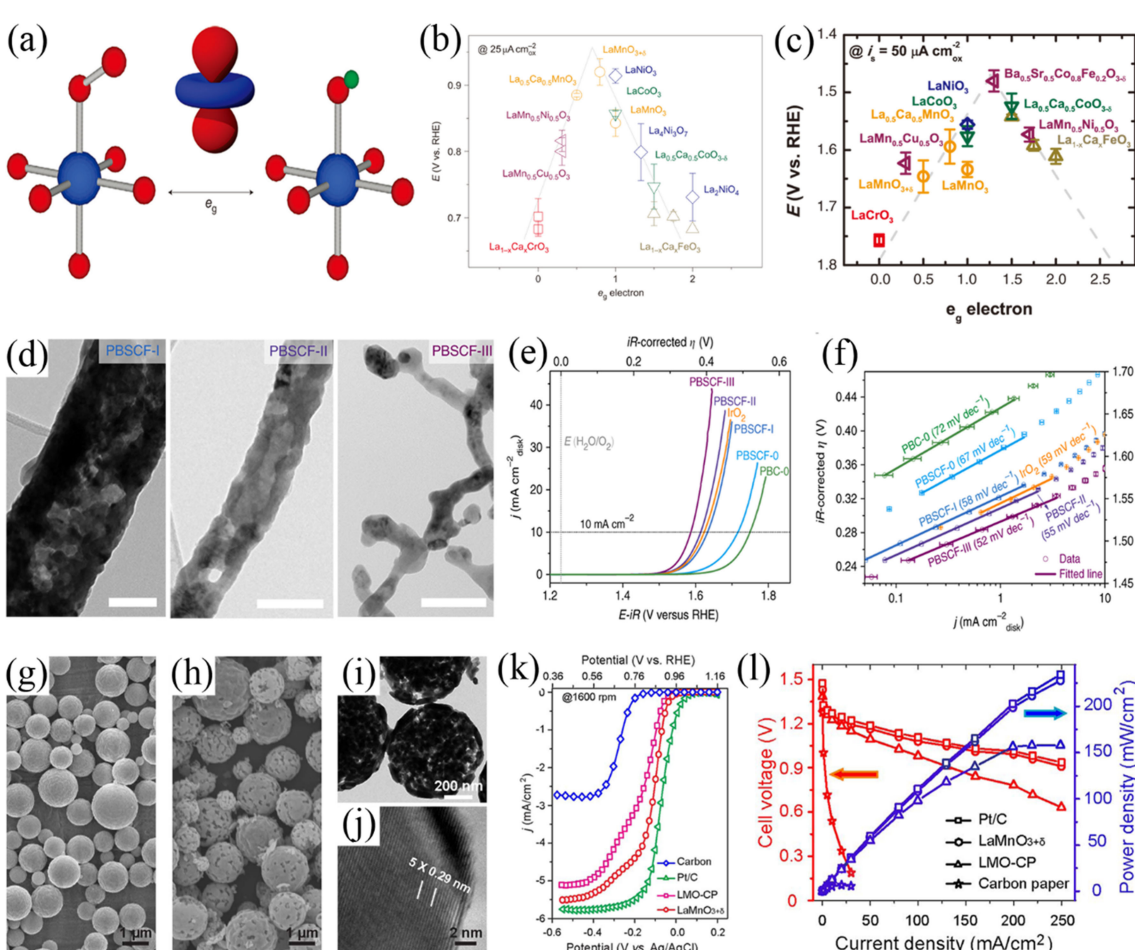


Figure 5. a) The graphic illustration of the e_g electron points directly towards the surface O atom. The red, blue and green balls represent O, B and H atoms respectively. b) Potentials at $25 \mu\text{A cm}^{-2}$ vs e_g orbital for perovskite-based oxides as ORR electrocatalysts. Reproduced with permission.^[87] Copyright 2011, Nature. c) The overpotentials at 50 mA cm^{-2} vs the occupancy of the e_g -symmetry electron of the metal in the B site for perovskite-based oxides as OER electrocatalysts. Reproduced with permission.^[88] Copyright 2011, Science. d) TEM images of PBSCF-I, PBSCF-II and PBSCF-III nanofibers. Capacitance- and ohmic resistance-corrected OER LSV curves (e) and Tafel plots (f) of IrO_2 , PBC, PBSCF powders and PBSCF nanofibers in 0.1 M KOH . Reproduced with permission.^[89] Copyright 2017, Nature. SEM images of LaMnO_3 precursor (g) and mesoporous $\text{LaMnO}_{3+\delta}$ product (h), TEM (i), and HRTEM (j) images of the mesoporous $\text{LaMnO}_{3+\delta}$ microspheres. k) LSV curves of the mesoporous $\text{LaMnO}_{3+\delta}$ microspheres measured in O_2 -saturated 0.1 M KOH solution. l) I–V and I–P results of Zn-air batteries with bare, mesoporous $\text{LaMnO}_{3+\delta}$, LMO-CP and Pt/C loaded gas diffusion electrodes. The electrolyte employed was 6 M KOH . Reproduced with permission.^[92] Copyright 2018, Elsevier.

(Figure 5*l*) was reached, very close to the performance of Pt/C (1.47 V and 202.8 mWcm⁻²).

4. Metal Oxide/Carbon Hybrids

The major drawback of metal oxides as OER/ORR electrocatalysts is their poor electric conductivity. Introduction of carbon materials has been spotlighted as a vital strategy to enhance the electron transportation between electrocatalysts and supporting electrodes. At the same time, it can drastically improve the performance of the oxide catalysts itself.^[93,94] For example, flower-like δ-MnO₂ deposited on the surface of 3D graphene shows a much higher bifunctional activity compared with the carbon free MnO₂ counterpart.^[95] When used in Li-air battery assemblies, a discharge capacity as high as 3660 mAhg⁻¹ could be achieved, and the energy density showed a very high average value of 1350 WhKg⁻¹ during 110 cycles. Similar effects could be found in composites of δ-MnO₂ and Co₃O₄ with other carbon materials.^[96–99] Also the loading of electrocatalysts on carbon supports has a major influence on the battery performance. For example, adjusting the CoFe₂O₄ loading on carbon support from 3.7 to 8.1 and 16.4 wt %, the discharge capacities of the fabricated Li-air coin-cells was increased from 3390 to 6650 and 7510 mAhg_(carbon + CoFe2O4)⁻¹.^[100]

Heteroatom (e.g., N, S, and P) doping into carbon materials can further increase the activity of the air electrodes via synergistic effects resulting from enhanced conductivity and increased nucleation sites.^[101–106] Cho et al. prepared Mn_xCo_{3-x}O₄/N-doped Ketjen black composites (Figure 6a).^[107] Compared with the pristine samples, the N-doped material showed a more positive onset potential and smaller Tafel slope for ORR (Figure 6b and c).

High potentials applied during the OER process can lead to the corrosion of carbon materials, and thereby lead to poor durability of the battery systems.^[108,109] Graphitic carbon materials such as carbon nanotubes and graphene display a higher corrosion resistance compared to amorphous carbon. Thus, composite materials based on graphitic carbon have a higher potential for providing enhanced catalytic stability.^[110–112]

Metal ions and graphitic carbon materials can also have a strong beneficial coupling effect.^[113,114] Hybrids of atomically thin porous Co₃O₄ nanosheets and N-doped reduced graphene oxide (N-rGO) showed enhanced ORR and OER performance compared to pristine Co₃O₄ nanosheets and N-rGO, separately (Figure 6d–e).^[115] When used in flexible fiber-shaped Zn-air battery assemblies, the catalyst exhibited a relatively large volumetric energy density of 36.1 mWhcm⁻³ and a better stability than the mixture of commercial Pt/C and RuO₂ (Figure 6f). Apart from that, Chen et al. prepared a hybrid of metallic Co and spinel Co₃O₄, encapsulated by porous graphitized shells (Co/Co₃O₄@PGS) (Figure 6g).^[116] The composite exhibited excellent bifunctional catalytic activity, which is even better than commercial precious metal catalysts (Figure 6h). In full Zn-air battery cells, it can output a power density of as high as 118.27 mWcm⁻² and ultra-long cycling life of 800 h, much superior to the Zn-air battery made of Pt/C and IrO₂ (Figure 6i–

k). Besides, also the ratio of TMOs and carbon materials is of great importance.^[117,118] For instance, MnCo₂O₄ nanoparticles with a loading of 50% on nitrogen-doped macroporous carbon nanofiber arrays displayed better bifunctional activity than observed for composites with a 30% and 70% TMO loading.^[106]

In addition, the porous structure of the air electrode integrated electrocatalysts is of great significance to the overall battery performance. Hybridization with carbon materials could significantly improve the porosity of TMO catalysts. Nevertheless, it can react with the produced Li₂O₂ and form carbonates when used in Li-air batteries. These carbonates could clog the pores and reduce the electric conductivity of the air electrode. Employing some specific TMOs, the carbonate formation can be alleviated. For example, Li₂O₂ was inclined to grow on the Co/CoO nanoparticles rather than the carbon material, thus the use of Co/CoO in Li-air battery could result in an increased battery capacity from 4100 to 7800 mAh g⁻¹.^[119]

5. Conclusions and Outlook

Because of their ultra-high energy densities, Li-air and Zn-air batteries are promising energy storage and conversion devices. Despite great progress has been made in recent years, further investigations should be performed to facilitate their practical applications. As the most potential electrocatalysts for Li-air and Zn-air batteries, TMOs exhibit low cost as well as high bifunctional activity for both ORR and OER (Table 1–2). This work has highlighted the recent experimental and theoretical advances in terms of Li-air and Zn-air batteries, which employ TMOs as bifunctional oxygen electrocatalysts. The purpose of this summary is to provide valuable insight and inspiration to help to promote the development and application of transition metal oxides in metal-air batteries.

The performance of a metal-air batteries can be influenced by the activity of oxygen catalysts, the configuration of the battery, the structure of the air electrodes, and the type of the electrolyte used. Indeed, the decline of battery performance caused by the last three factors can be prevented by choosing proper species or optimizing the physicochemical properties of the electrocatalysts. For example, using TMOs as an oxygen catalyst could avoid the inactivation induced by electrochemical processes involving oxygen species at high potentials in two-electrode configuration batteries. Additionally, side effects caused by additives can be avoided by directly integrating the electrocatalysts into the air electrode. Increasing the porosity and optimizing the adsorption of produced precipitates could maintain the accessibility of the catalytically active area.

For improving the bifunctional activity of oxygen electrocatalysts, the utmost challenge is to balance their ORR and OER performance. For TMOs, Co₃O₄ and perovskite oxides always show better OER performance, while MnO₂ based catalysts exhibit better ORR activity. Nonetheless, the activity for both, ORR and OER can be simultaneously improved for TMO catalysts. In general, the number of accessible active sites, fluent mass transport and electronic conductivity of the catalysts are key parameters for the activity of electrocatalysts.

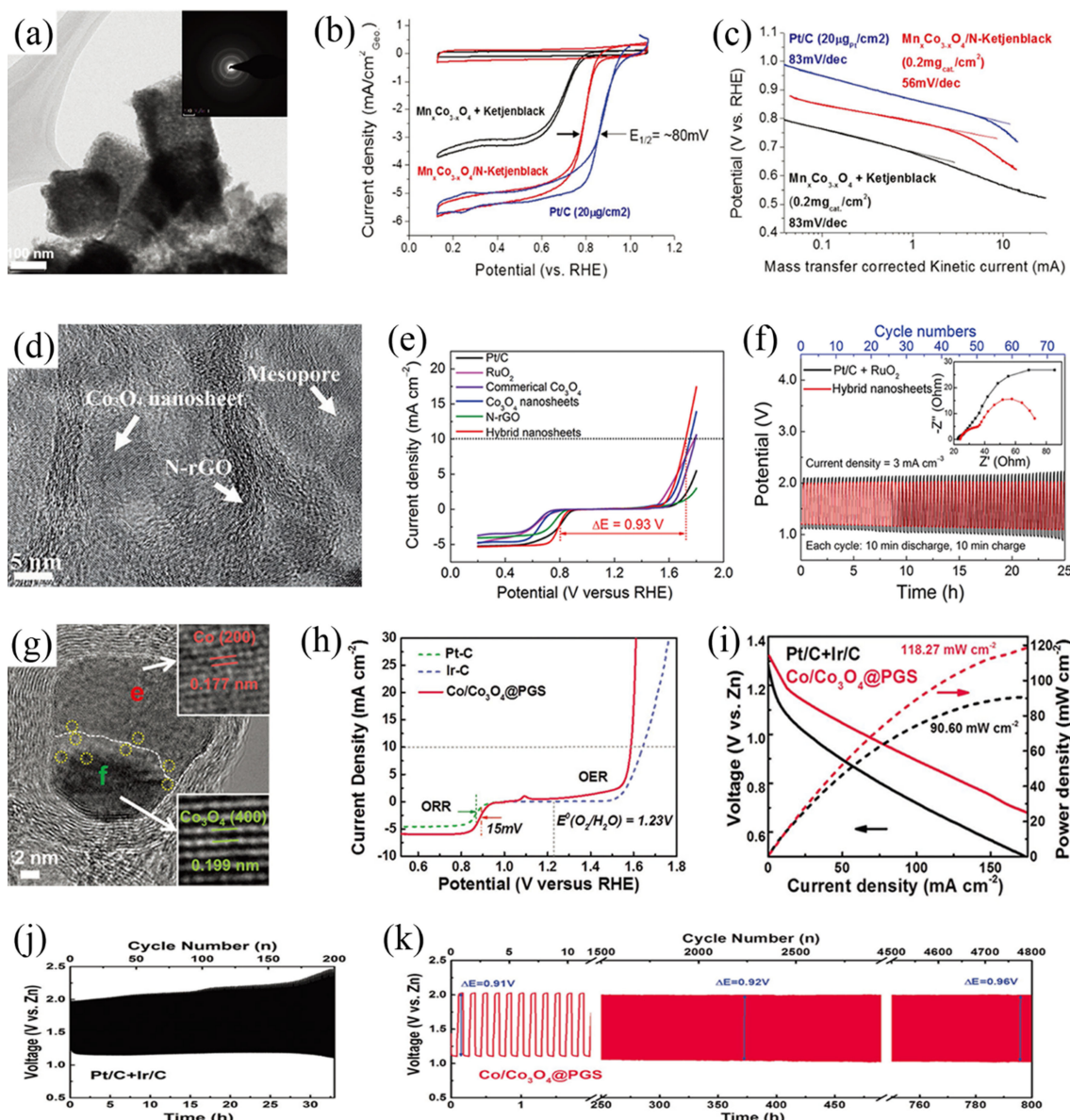


Figure 6. TEM image (a), CV curve (b) and Tafel plots (c) of $\text{Mn}_{x}\text{Co}_{3-x}\text{O}_4/\text{N}$ -doped ketjenblack in O_2 saturated 0.1 M KOH. Reproduced with permission.^[107] Copyright 2016, Wiley. TEM image (d), ORR and OER polarization curves (e) of thin porous Co_3O_4 layers/N-rGO in 0.1 M KOH. f) Discharge and charge polarization curve of the flexible Zn-air batteries. The electrolyte was alkaline gel electrolyte made by 0.15 M KOH and PVA. Reproduced with permission.^[115] Copyright 2018, Wiley. TEM image (g) and bifunctional activity performance (h) of $\text{Co}/\text{Co}_3\text{O}_4@\text{PGS}$. Charge/discharge curves (i) and stability performances of Zn-air battery based on Pt/C+Ir/C (j) and $\text{Co}/\text{Co}_3\text{O}_4@\text{PGS}$ (k) at 10 mA cm^{-2} . The electrolytes for the catalytic activity tests and batteries performance measurements were 0.1 M KOH and a mixture solution of 6.0 M KOH and 0.2 M $\text{Zn}(\text{CH}_3\text{COO})_2$, respectively. Reproduced with permission.^[116] Copyright 2018, Wiley.

For instance, the ORR and OER activity of TMOs can be enhanced by the exposition of cations in different valence states to optimize the adsorption of intermediates of the two reactions. Different phases and exposed crystal faces of specific TMOs exhibit diverse intrinsic activity. Thus, facilitating synthetic access to suitable phases as well as exposed faces is an absolutely necessary step for the design of efficient electrocatalysts. Constructing electrodes of specific morphology is an effective way to increase the number of accessible active sites and to facilitate mass transport during the electrocatalytic reactions.

Doping will not only result in the introduction of more active sites, but is also leading to an optimization of the decomposition of metal oxides formed during the charging process of Li-air and Zn-air batteries. Hybridizing TMO catalysts with doped graphene or carbon nanotubes can simultaneously lead to enhanced conductivity and enlarged specific surface area and the formation of carbonates is avoided, thus improving the battery performance and stability.

Although research to date has considerably improved the performance of transition metal oxides as bifunctional oxygen catalysts used in metal-air batteries, more in-depth experimental and theoretical research is still needed to promote their

Table 1. TMO-based electrocatalyst performance in rechargeable Li-air batteries.^[a]

Electrocatalyst	ORR activity	OER activity	Battery performance	Electrolyte	Reference
RuO ₂ /MnO ₂ /CNTs	Onset potential: 0.83 V	31.1 mA cm ⁻² at 1.8 V	600 mAh g ⁻¹	1 M LiTFSI in TEGDME	54
β-MnO ₂ nanowires	–	–	~2500 mAh g ⁻¹	1 M LiTFSI in TEGDME	57
Li ₂ MnO ₃	–	–	5000 mAh g ⁻¹	1 M LiPF ₆ in PC	68
Porous NiCo ₂ O ₄ microspheres	–	–	6822 mAh g _{carbon} ⁻¹	1 M LiTFSI in TEGDME	75
Pt/C (ORR); NiCo ₂ O ₄ nanosheet (OER)	–	–	50 cycles at 0.5 mA cm ⁻²	1 M LiPF ₆ in EC/DEC (1:1 v/v)	77
FeCo ₂ O ₄ porous rods	–	–	2350 mAh g ⁻¹ ; 40 cycles	1 M LiTFSI in TEGDME	80
Spinel CuCo ₂ O ₄ nanocrystals	–	–	50 cycles at 100 mA g ⁻¹	1 M LiTFSI in TEGDME	79
NiMn ₂ O ₄ of intermediate spinel structure	–	–	~940 mAh g ⁻¹	1 M LiTFSI in TEGDME	81
CoMn ₂ O ₄ nanostructure	–	–	5355 mAh g _{carbon} ⁻¹ at 100 mA g _{carbon} ⁻¹	1 M LiTFSI in TEGDME	83
Flower-like δ-MnO ₂ /3D graphene	–	–	3660 mAh g ⁻¹ ; 132 cycles	0.1 M LiClO ₄ in DME	95
Carbonized Co ₃ O ₄ inverse opals	Half-wave potential: 0.7 V	10 mA cm ⁻² at 1.71 V	6959 mAh g ⁻¹	1 M LiTFSI in TEGDME	98
MCNTs@MnO ₂ nanocomposite	–	–	5.4 mAh cm ⁻² ; 300 cycles at 500 mA g ⁻¹	1 M LiTFSI in TEGDME	99
CoFe ₂ O ₄ supported on Vulcan XC-72	–	–	7510 mAh g _(carbon + CoFe2O4) ⁻¹	0.1 M LiPF ₆ in DMSO	100
3D Co/CoO-Graphene-Carbonized Melamine Foam	–	–	7800 mAh g ⁻¹	1 M LiCF ₃ SO ₃ in TEGDME	119

^[a] The detail test condition refers to the primary references.
Table 2. TMO-based electrocatalyst performance in rechargeable Zn-air batteries.^[b]

Electrocatalyst	ORR activity	OER activity	Battery performance	Electrolyte	Reference
Co ₃ O ₄ nanopolyhedron /N-rGO	Onset potential: 0.89 V vs RHE; Tafel slop: 62 mV dec ⁻¹	Tafel slop: 62 mV dec ⁻¹	Open-circuit voltage: 1.51 V; Power density: 118 mW cm ⁻² ; Specific discharge capacity: 786 mAh g ⁻¹	6.0 M KOH + 0.2 M Zn(ac) ₂	47
N-Co ₃ O ₄ mesoporous nanowire arrays	Onset potential: 0.94 V vs RHE; Tafel slop: 57.6 mV dec ⁻¹	–	Volumetric capacity: 98.1 mAh cm ⁻³ ; Peak power density: 32.0 mW cm ⁻³	KOH + PVA	48
Mg-Co ₃ O ₄ double shell hollow spheres	Onset potential: 0.925 V vs RHE; Tafel slop: 59 mV dec ⁻¹	Tafel slop: 52 mV dec ⁻¹	Power density: 125 mW cm ⁻²	6.0 M KOH + 0.2 M Zn(ac) ₂	49
3D ordered porous Co ₃ O ₄	Onset potential: -0.197 V vs SCE; Half-wave potential: -0.360 V vs SCE; n=3.9	Onset potential: 0.561 V vs SCE	Open-circuit voltage: 1.36 V; Stability: 300 cycles at 10 mA cm ⁻²	6.0 M KOH + 0.2 M Zn(ac) ₂	53
Mesoporous LaMnO _{3+δ} perovskite spheres	Half-wave potential: 0.852 V vs RHE; n=3.95	–	Open-circuit voltage: 1.43 V; Power density: 198.6 mW cm ⁻²	6.0 M KOH	67
Hierarchical nano-structured NiCo ₂ O ₄ PrBa _{0.5} Sr _{0.5} Co _{2-x} Fe _x O _{5+δ} nanofibers	Onset potential: 0.93 V vs RHE Tafel slop: 98 mV dec ⁻¹	Tafel slop: 87 mV dec ⁻¹ Onset potential: 1.52 V vs RHE; Tafel slop: 81 mV dec ⁻¹	Open-circuit voltage: 1.45 V; Discharge capacity: ~580 mAh g ⁻¹ Power density: 127 mW cm ⁻² ; Stability: 150 cycles at 10 mA cm ⁻²	6.0 M KOH	76
N-doped carbon (ORR); Co ₃ O ₄ @Ni(OER)	Half-wave potential: -0.188 V vs Ag/AgCl; n=4	Tafel slop: 23 mV dec ⁻¹	Stability: 200 cycles (800 h) at 10 mA cm ⁻²	6.0 M KOH	97
Co ₃ O ₄ / carbon nanofibers	–	–	Cycling ability: 110 cycles	6.0 M KOH + 0.2 M Zn(ac) ₂	96
Co ₃ O ₄ nanosheets/N-rGO	Onset potential: 0.92 V vs RHE	E _{i=10} : 1.72 V; Tafel slop: 101 mV dec ⁻¹	Volumetric energy density: 36.1 mWh cm ⁻³	0.15 M KOH + PVA	115
Co/Co ₃ O ₄ @PGS	Onset potential: 0.97 V vs RHE	E _{i=10} : 1.58 V; Tafel slop: 76.1 mV dec ⁻¹	Power density: 118.27 mW cm ⁻² ; stability: 800 h	6.0 M KOH + 0.2 M Zn(ac) ₂	116

^[b] The detail test condition refers to the primary references.

practical application. Firstly, the design principles of the active TMOs as bifunctional oxygen catalysts should be investigated with the support of theoretical screening in order to connect the activity of the catalysts with experimental conditions.

Secondly, to acquire high-performance metal-air batteries, the combination of theoretical calculations and experimental results is required to understand operation principles of the oxide catalysts in the batteries, and especially the relationship

between the catalysts' properties and the battery performance. Finally, for practical applications of TMOs in metal-air batteries, the cost, abundance of the resources, and even the operation administration system should be taken into consideration. Overall, TMOs show great potential as effective and bifunctional catalysts for the complicated oxygen redox electrochemistry, yet there is still a long way to go. Endeavors should be made to promote their practical application in Li-air and Zn-air batteries.

Acknowledgements

This work is financially supported by National 1000 Young Talents Program of China. The Fundamental Research Funds for the Central Universities (2018KFYXJC044, 2018KFYYXJJ121, 2017KFXKJC002, 2017KFYXJJ164) and the Innovation Foundation of Shenzhen Government (JCYJ20160408173202143) are also acknowledged.

Conflict of Interest

The authors declare no conflict of interest.

Keywords: bifunctional electrocatalysts • materials science • metal-air batteries • oxygen redox electrochemistry • transition metal oxides

- [1] K. B. Karnauskas, J. K. Lundquist, L. Zhang, *Nat. Geosci.* **2018**, *11*, 38–43.
- [2] J. Pan, Y. Y. Xu, H. Yang, Z. Dong, H. Liu, B. Y. Xia, *Adv. Sci.* **2018**, *5*, 1700691.
- [3] S. Li, C. Cheng, X. Zhao, J. Schmidt, A. Thomas, *Angew. Chem. Int. Ed.* **2018**, *57*, 1856–1862; *Angew. Chem.* **2018**, *130*, 1874–1880.
- [4] F. Y. Cheng, J. Chen, *Chem. Soc. Rev.* **2012**, *41*, 2172–2192.
- [5] Y. G. Li, H. J. Dai, *Chem. Soc. Rev.* **2014**, *43*, 5257–5275.
- [6] P. Gu, M. B. Zheng, Q. X. Zhao, X. Xiao, H. G. Xue, H. Pang, *J. Mater. Chem. A* **2017**, *5*, 7651–7666.
- [7] K. Huang, *Angew. Chem. Int. Ed.* **2017**, *56*, 12826–12827; *Angew. Chem.* **2017**, *129*, 13002–13004.
- [8] X. Y. Yang, J. J. Xu, Z. W. Chang, D. Bao, Y. B. Yin, T. Liu, J. M. Yan, D. P. Liu, Y. Zhang, X. B. Zhang, *Adv. Energy Mater.* **2018**, *8*, 1702242.
- [9] Y. Liu, P. He, H. Zhou, *Adv. Energy Mater.* **2018**, *8*, 1701602.
- [10] I. S. Amiinu, X. Liu, Z. Pu, W. Li, Q. Li, J. Zhang, H. Tang, H. Zhang, S. Mu, *Adv. Funct. Mater.* **2018**, *28*, 1704638.
- [11] M. Zhang, Q. Dai, H. Zheng, M. Chen, L. Dai, *Adv. Mater.* **2018**, *30*, 1705431.
- [12] X. L. Tian, L. Wang, P. Deng, Y. Chen, B. Y. Xia, *J. Energy Chem.* **2017**, *26*, 1067–1076.
- [13] X. L. Tian, Y. Y. Xu, W. Zhang, T. Wu, B. Y. Xia, X. Wang, *ACS Energy Lett.* **2017**, *2*, 2035–2043.
- [14] M. Sevim, T. Şener, Ö. Metin, *Int. J. Hydrogen Energy* **2015**, *40*, 10876–10882.
- [15] M. Sevim, C. Francia, J. Amici, S. Vankova, T. Şener, Ö. Metin, *J. Alloys Compd.* **2016**, *683*, 231–240.
- [16] X. Wang, B. Xia, Y. Yan, M. Miao, J. Pan, T. He, *Chem. Eur. J.* **2017**, *23*, 10947–10961.
- [17] J. Zhang, M. Ren, L. Wang, Y. Li, B. I. Yakobson, J. M. Tour, *Adv. Mater.* **2018**, *30*, 1707319.
- [18] H.-F. Wang, C. Tang, Q. Zhang, *Catal. Today* **2018**, *301*, 25–31.
- [19] H. Li, Q. Li, P. Wen, T. B. Williams, S. Adhikari, C. Dun, C. Lu, D. Itanze, L. Jiang, D. L. Carroll, *Adv. Mater.* **2018**, *30*, 1705796.
- [20] X. L. Tian, L. Wang, B. Chi, Y. Xu, S. Zaman, K. Qi, H. Liu, S. Liao, B. Y. Xia, *ACS Catal.* **2018**, *8*, 8970–8975.

- [21] N. D. Leonard, S. Wagner, F. Luo, J. Steinberg, W. Ju, N. Weidler, H. Wang, U. I. Kramm, P. Strasser, *ACS Catal.* **2018**, *8*, 1640–1647.
- [22] X. Xu, F. Song, X. Hu, *Nat. Commun.* **2016**, *7*, 12324.
- [23] M. Chen, L. Wang, H. Yang, S. Zhao, H. Xu, G. Wu, *J. Power Sources* **2018**, *375*, 277–290.
- [24] W. Xia, A. Mahmood, Z. Liang, R. Zou, S. Guo, *Angew. Chem. Int. Ed.* **2016**, *55*, 2650–2676; *Angew. Chem.* **2016**, *128*, 2698–2726.
- [25] M. Wang, T. Qian, S. Liu, J. Zhou, C. Yan, *ACS Appl. Mater. Interfaces* **2017**, *9*, 21216–21224.
- [26] S. Kang, Y. Mo, S. P. Ong, G. Ceder, *Nano Lett.* **2014**, *14*, 1016–1020.
- [27] C. O. Laiore, S. Mukerjee, K. Abraham, E. J. Plachta, M. A. Hendrickson, *J. Phys. Chem. C* **2010**, *114*, 9178–9186.
- [28] R. Black, S. H. Oh, J.-H. Lee, T. Yim, B. Adams, L. F. Nazar, *J. Am. Chem. Soc.* **2012**, *134*, 2902–2905.
- [29] F. Li, T. Zhang, H. Zhou, *Energy Environ. Sci.* **2013**, *6*, 1125–1141.
- [30] D. Xu, Z.-I. Wang, J.-J. Xu, L.-I. Zhang, L.-m. Wang, X.-b. Zhang, *Chem. Commun.* **2012**, *48*, 11674–11676.
- [31] W. Vielstich, H. Yokokawa, H. A. Gasteiger, *Handbook of fuel cells: fundamentals technology and applications*, John Wiley & Sons **2009**.
- [32] V. Neburchilov, H. Wang, J. J. Martin, W. Qu, *J. Power Sources* **2010**, *195*, 1271–1291.
- [33] A. Kraysberg, Y. Ein-Eli, *J. Power Sources* **2011**, *196*, 886–893.
- [34] M. Kuang, G. Zheng, *Small* **2016**, *12*, 5656–5675.
- [35] J. Fu, Z. P. Cano, M. G. Park, A. Yu, M. Fowler, Z. Chen, *Adv. Mater.* **2017**, *29*, 1–34.
- [36] E. Davari, D. Ivey, *Energy Fuels* **2018**, *2*, 39–67.
- [37] D. Yang, L. Zhang, X. Yan, X. Yao, *Small Methods* **2017**, *1*, 1700209.
- [38] Z. W. Seh, J. Kibsgaard, C. F. Dickens, I. B. Chorkendorff, J. K. Norskov, T. F. Jaramillo, *Science* **2017**, *355*, 146.
- [39] I. C. Man, H. Y. Su, F. Calle-Vallejo, H. A. Hansen, J. I. Martínez, N. G. Inoglu, J. Kitchin, T. F. Jaramillo, J. K. Nørskov, J. Rossmeisl, *ChemCat-Chem* **2011**, *3*, 1159–1165.
- [40] A. Débart, J. Bao, G. Armstrong, P. G. Bruce, *J. Power Sources* **2007**, *174*, 1177–1182.
- [41] J. S. Lee, S. Tai Kim, R. Cao, N. S. Choi, M. Liu, K. T. Lee, J. Cho, *Adv. Energy Mater.* **2011**, *1*, 34–50.
- [42] R. Cao, J. S. Lee, M. Liu, J. Cho, *Adv. Energy Mater.* **2012**, *2*, 816–829.
- [43] H. C. Li, Y. J. Zhang, X. Hu, W. J. Liu, J. J. Chen, H. Q. Yu, *Adv. Energy Mater.* **2018**, *8*, 1702734.
- [44] D. U. Lee, P. Xu, Z. P. Cano, A. G. Kashkooli, M. G. Park, Z. Chen, *J. Mater. Chem. A* **2016**, *4*, 7107–7134.
- [45] X. He, F. Yin, G. Li, *Int. J. Hydrogen Energy* **2015**, *40*, 9713–9722.
- [46] Z. Lu, H. Wang, D. Kong, K. Yan, P.-C. Hsu, G. Zheng, H. Yao, Z. Liang, X. Sun, Y. Cui, *Nat. Commun.* **2014**, *5*, 4345.
- [47] X. Han, G. He, Y. He, J. Zhang, X. Zheng, L. Li, C. Zhong, W. Hu, Y. Deng, T. Y. Ma, *Adv. Energy Mater.* **2018**, *8*, 1870043.
- [48] M. Yu, Z. Wang, C. Hou, Z. Wang, C. Liang, C. Zhao, Y. Tong, X. Lu, S. Yang, *Adv. Mater.* **2017**, *29*, 1602868.
- [49] Y.-P. Deng, Y. Jiang, D. Luo, J. Fu, R. Liang, S. Cheng, Z. Bai, Y. Liu, W. Lei, L. Yang, *ACS Energy Lett.* **2017**, *2*, 2706–1712.
- [50] T. Ling, D.-Y. Yan, Y. Jiao, H. Wang, Y. Zheng, X. Zheng, J. Mao, X.-W. Du, Z. Hu, M. Jaroniec, *Nat. Commun.* **2016**, *7*, 12876.
- [51] Y. Wang, T. Zhou, K. Jiang, P. Da, Z. Peng, J. Tang, B. Kong, W. B. Cai, Z. Yang, G. Zheng, *Adv. Energy Mater.* **2014**, *4*, 1400696.
- [52] W. B. Luo, X. W. Gao, S. L. Chou, Y. M. Kang, J. Z. Wang, H. K. Liu, S. X. Dou, *Adv. Energy Mater.* **2017**, *7*, 1700234.
- [53] M. G. Park, D. U. Lee, M. H. Seo, Z. P. Cano, Z. W. Chen, *Small* **2016**, *12*, 2707–2714.
- [54] Y. J. Lee, S. H. Park, S. H. Kim, Y. Ko, K. Kang, Y. J. Lee, *ACS Catal.* **2018**, *8*, 2923–2934.
- [55] I. Katsounaras, S. Cherevko, A. R. Zeradjanin, K. J. Mayrhofer, *Angew. Chem. Int. Ed.* **2014**, *53*, 102–121.
- [56] Y. Meng, W. Song, H. Huang, Z. Ren, S.-Y. Chen, S. L. Suib, *J. Am. Chem. Soc.* **2014**, *136*, 11452–11464.
- [57] O. Oloniyi, S. Kumar, K. Scott, *J. Electron. Mater.* **2012**, *41*, 921–927.
- [58] F. Cheng, T. Zhang, Y. Zhang, J. Du, X. Han, J. Chen, *Angew. Chem. Int. Ed.* **2013**, *52*, 2474–2477.
- [59] T. N. Lambert, J. A. Vigil, S. E. White, C. J. Delker, D. J. Davis, M. Kelly, M. T. Brumbach, M. A. Rodriguez, B. S. Swartzentruber, *J. Phys. Chem. C* **2017**, *121*, 2789–2797.
- [60] T. Zhang, F. Cheng, J. Du, Y. Hu, J. Chen, *Adv. Energy Mater.* **2015**, *5*, 1400654.
- [61] Y. Zhao, C. Chang, F. Teng, Y. Zhao, G. Chen, R. Shi, G. I. Waterhouse, W. Huang, T. Zhang, *Adv. Energy Mater.* **2017**, *7*, 1700005.

- [62] T. Takashima, K. Hashimoto, R. Nakamura, *J. Am. Chem. Soc.* **2012**, *134*, 1519–1527.
- [63] R. Frydendal, E. A. Paoli, I. Chorkendorff, J. Rossmeisl, I. E. Stephens, *Adv. Energy Mater.* **2015**, *5*, 1500991.
- [64] A. Ramírez, P. Hillebrand, D. Stellmach, M. M. May, P. Bogdanoff, S. Fiechter, *J. Phys. Chem. C* **2014**, *118*, 14073–14081.
- [65] W. Wang, J. Geng, L. Kuai, M. Li, B. Geng, *Chem. Eur. J.* **2016**, *22*, 9909–9913.
- [66] H.-Y. Su, Y. Gorlin, I. C. Man, F. Calle-Vallejo, J. K. Nørskov, T. F. Jaramillo, J. Rossmeisl, *Phys. Chem. Chem. Phys.* **2012**, *14*, 14010–14022.
- [67] F. Jiao, H. Frei, *Energy Environ. Sci.* **2010**, *3*, 1018–1027.
- [68] L. Trahey, N. K. Karan, M. K. Chan, J. Lu, Y. Ren, J. Greeley, M. Balasubramanian, A. K. Burrell, L. A. Curtiss, M. M. Thackeray, *Adv. Energy Mater.* **2013**, *3*, 75–84.
- [69] J. Park, M. Risch, G. Nam, M. Park, T. J. Shin, S. Park, M. G. Kim, Y. Shao-Horn, J. Cho, *Energy Environ. Sci.* **2017**, *10*, 129–136.
- [70] Y. Yan, B. Y. Xia, B. Zhao, X. Wang, *J. Mater. Chem. A* **2016**, *4*, 17587–17603.
- [71] F. Cheng, J. Shen, B. Peng, Y. Pan, Z. Tao, J. Chen, *Nat. Chem.* **2011**, *3*, 79.
- [72] C. Li, X. Han, F. Cheng, Y. Hu, C. Chen, J. Chen, *Nat. Commun.* **2015**, *6*, 7345.
- [73] G. Wu, J. Wang, W. Ding, Y. Nie, L. Li, X. Qi, S. Chen, Z. Wei, *Angew. Chem. Int. Ed.* **2016**, *55*, 1340–1344.
- [74] H. Yang, F. Hu, Y. Zhang, L. Shi, Q. Wang, *Nano Res.* **2016**, *9*, 207–213.
- [75] S. Peng, Y. Hu, L. Li, X. Han, F. Cheng, M. Srinivasan, Q. Yan, S. Ramakrishna, J. Chen, *Nano Energy* **2015**, *13*, 718–726.
- [76] M. Prabu, K. Ketpang, S. Shanmugam, *Nanoscale* **2014**, *6*, 3173–3181.
- [77] L. Li, A. Manthiram, *Nano Energy* **2014**, *9*, 94–100.
- [78] T. Maiyalagan, K. A. Jarvis, S. Therese, P. J. Ferreira, A. Manthiram, *Nat. Commun.* **2014**, *5*, 3949.
- [79] Y. Liu, L.-J. Cao, C.-W. Cao, M. Wang, K.-L. Leung, S.-S. Zeng, T. Hung, C. Chung, Z.-G. Lu, *Chem. Commun.* **2014**, *50*, 14635–14638.
- [80] S. G. Mohamed, Y.-Q. Tsai, C.-J. Chen, Y.-T. Tsai, T.-F. Hung, W.-S. Chang, R.-S. Liu, *ACS Appl. Mater. Interfaces* **2015**, *7*, 12038–12046.
- [81] S. Li, J. Xu, Z. Ma, S. Zhang, X. Wen, X. Yu, J. Yang, Z.-F. Ma, X. Yuan, *Chem. Commun.* **2017**, *53*, 8164–8167.
- [82] Y. Liang, H. Wang, J. Zhou, Y. Li, J. Wang, T. Regier, H. Dai, *J. Am. Chem. Soc.* **2012**, *134*, 3517–3523.
- [83] S. Peng, L. Li, Y. Hu, M. Srinivasan, F. Cheng, J. Chen, S. Ramakrishna, *ACS Nano* **2015**, *9*, 1945–1954.
- [84] R. Mohamed, X. Cheng, E. Fabbri, P. Levecque, R. Kötz, O. Conrad, T. J. Schmidt, *J. Electrochem. Soc.* **2015**, *162*, F579–F586.
- [85] F. Wang, I. Grinberg, A. M. Rappe, *Appl. Phys. Lett.* **2014**, *104*, 152903.
- [86] J. Hwang, R. R. Rao, L. Giordano, Y. Katayama, Y. Yu, Y. Shao-Horn, *Science* **2017**, *358*, 751–756.
- [87] J. Suntivich, H. A. Gasteiger, N. Yabuuchi, H. Nakanishi, J. B. Goodenough, Y. Shao-Horn, *Nat. Chem.* **2011**, *3*, 546–550.
- [88] J. Suntivich, K. J. May, H. A. Gasteiger, J. B. Goodenough, Y. Shao-Horn, *Science* **2011**, *334*, 1383–1385.
- [89] B. Zhao, L. Zhang, D. Zhen, S. Yoo, Y. Ding, D. Chen, Y. Chen, Q. Zhang, B. Doyle, X. Xiong, *Nat. Commun.* **2017**, *8*, 14586.
- [90] Y. Bu, O. Gwon, G. Nam, H. Jang, S. Kim, Q. Zhong, J. Cho, G. Kim, *ACS Nano* **2017**, *11*, 11594–11601.
- [91] W. T. Hong, K. A. Stoerzinger, Y.-L. Lee, L. Giordano, A. Grimaud, A. M. Johnson, J. Hwang, E. J. Crumlin, W. Yang, Y. Shao-Horn, *Energy Environ. Sci.* **2017**, *10*, 2190–2200.
- [92] L. Kuai, E. Kan, W. Cao, M. Huttula, S. Olliikkala, T. Ahopelto, A.-P. Honkanen, S. Huotari, W. Wang, B. Geng, *Nano Energy* **2018**, *43*, 81–90.
- [93] H. Wang, H. Dai, *Chem. Soc. Rev.* **2013**, *42*, 3088–3113.
- [94] X. Han, F. Cheng, C. Chen, Y. Hu, J. Chen, *Nano Res.* **2015**, *8*, 156–164.
- [95] S. Liu, Y. Zhu, J. Xie, Y. Huo, H. Y. Yang, T. Zhu, G. Cao, X. Zhao, S. Zhang, *Adv. Energy Mater.* **2014**, *4*, 1301960.
- [96] B. Li, X. Ge, F. T. Goh, T. A. Hor, D. Geng, G. Du, Z. Liu, J. Zhang, X. Liu, Y. Zong, *Nanoscale* **2015**, *7*, 1830–1838.
- [97] L. Li, C. Liu, G. He, D. Fan, A. Manthiram, *Energy Environ. Sci.* **2015**, *8*, 3274–3282.
- [98] S. A. Cho, Y. J. Jang, H. D. Lim, J. E. Lee, Y. H. Jang, T. T. H. Nguyen, F. M. Mota, D. P. Fenning, K. Kang, Y. Shao-Horn, *Adv. Energy Mater.* **2017**, *7*, 1700391.
- [99] X. Hu, J. Wang, Z. Li, J. Wang, D. H. Gregory, J. Chen, *Nano Lett.* **2017**, *17*, 2073–2078.
- [100] T. Şener, E. Kayhan, M. Sevim, Ö. Metin, *J. Power Sources* **2015**, *288*, 36–41.
- [101] Y. Y. Liang, Y. G. Li, H. L. Wang, J. G. Zhou, J. Wang, T. Regier, H. J. Dai, *Nat. Mater.* **2011**, *10*, 780–786.
- [102] J. Masa, W. Xia, I. Sinev, A. Zhao, Z. Sun, S. Grützke, P. Weide, M. Muhler, W. Schuhmann, *Angew. Chem. Int. Ed.* **2014**, *53*, 8508–8512.
- [103] X. Cao, J. Wu, C. Jin, J. Tian, P. Strasser, R. Yang, *ACS Catal.* **2015**, *5*, 4890–4896.
- [104] L. Li, S. Liu, A. Manthiram, *Nano Energy* **2015**, *12*, 852–860.
- [105] X. Liu, M. Park, M. G. Kim, S. Gupta, X. Wang, G. Wu, J. Cho, *Nano Energy* **2016**, *20*, 315–325.
- [106] D. Bin, Z. Guo, A. G. Tamirat, Y. Ma, Y. Wang, Y. Xia, *Nanoscale* **2017**, *9*, 11148–11157.
- [107] J. S. Lee, G. Nam, J. Sun, S. Higashi, H. W. Lee, S. Lee, W. Chen, Y. Cui, J. Cho, *Adv. Energy Mater.* **2016**, *6*, 1601052.
- [108] H. Wang, Y. Yang, Y. Liang, G. Zheng, Y. Li, Y. Cui, H. Dai, *Energy Environ. Sci.* **2012**, *5*, 7931–7935.
- [109] C. Wang, Z. Zhao, X. Li, R. Yan, J. Wang, A. Li, X. Duan, J. Wang, Y. Liu, J. Wang, *ACS Appl. Mater. Interfaces* **2017**, *9*, 41273–41283.
- [110] A. Zhao, J. Masa, W. Xia, A. Maljusch, M.-G. Willinger, G. Clavel, K. Xie, R. Schlögl, W. Schuhmann, M. Muhler, *J. Am. Chem. Soc.* **2014**, *136*, 7551–7554.
- [111] H. Osgood, S. V. Devaguptapu, H. Xu, J. Cho, G. Wu, *Nano Today* **2016**, *11*, 601–625.
- [112] N. Xu, J. Qiao, Q. Nie, M. Wang, H. Xu, Y. Wang, X.-D. Zhou, *Catal. Today* **2017**, *10*, 20.
- [113] B. Liu, W. Xu, P. Yan, P. Bhattacharya, R. Cao, M. E. Bowden, M. H. Engelhard, C. M. Wang, J. G. Zhang, *ChemSusChem* **2015**, *8*, 3697–3703.
- [114] X. Li, Z. Niu, J. Jiang, L. Ai, *J. Mater. Chem. A* **2016**, *4*, 3204–3209.
- [115] Y. Li, C. Zhong, J. Liu, X. Zeng, S. Qu, X. Han, Y. Deng, W. Hu, J. Lu, *Adv. Mater.* **2018**, *30*, 1703657.
- [116] Y. Jiang, Y. P. Deng, J. Fu, D. U. Lee, R. Liang, Z. P. Cano, Y. Liu, Z. Bai, S. Hwang, L. Yang, *Adv. Energy Mater.* **2018**, *8*, 1702900.
- [117] J. Guan, Z. Zhang, J. Ji, M. Dou, F. Wang, *ACS Appl. Mater. Interfaces* **2017**, *9*, 30662–30669.
- [118] X. Wang, Y. Li, T. Jin, J. Meng, L. Jiao, M. Zhu, J. Chen, *Nano Lett.* **2017**, *17*, 7989–7994.
- [119] P. Zhang, R. Wang, M. He, J. Lang, S. Xu, X. Yan, *Adv. Funct. Mater.* **2016**, *26*, 1354–1364.

Manuscript received: August 20, 2018

Accepted Article published: October 4, 2018

Version of record online: October 30, 2018